

Neuromorphic Engineering in Wetware: Discriminating Acoustic Frequencies through Their Effects on Chemical Waves

Laura Tomassoli, Leonardo Silva-Dias, Milos Dolnik, Irving R. Epstein, Raimondo Germani, and Pier Luigi Gentili*



Cite This: *J. Phys. Chem. B* 2024, 128, 1241–1255



Read Online

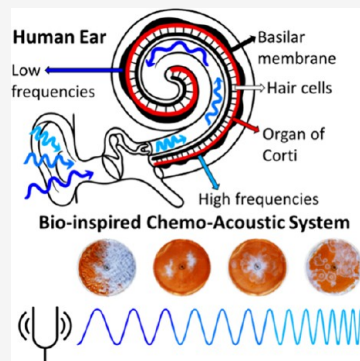
ACCESS |

Metrics & More

Article Recommendations

Supporting Information

ABSTRACT: Some features of the human nervous system can be mimicked not only through software or hardware but also through liquid solutions of chemical systems maintained under out-of-equilibrium conditions. We describe the possibility of exploiting a thin layer of the Belousov–Zhabotinsky (BZ) reaction as a surrogate for the cochlea for sensing acoustic frequencies. Experiments and simulations demonstrate that, as in the human ear where the cochlea transduces the mechanical energy of the acoustic frequencies into the electrochemical energy of neural action potentials and the basilar membrane originates topographic representations of sounds, our bioinspired chemoacoustic system, based on the BZ reaction, gives rise to spatiotemporal patterns as the representation of distinct acoustic bands through transduction of mechanical energy into chemical energy. Acoustic frequencies in the range 10–2000 Hz are partitioned into seven distinct bands based on three attributes of the emerging spatiotemporal patterns: (1) the types and frequencies of the chemical waves, (2) their velocities, and (3) the Faraday waves' wavelengths.



INTRODUCTION

Artificial intelligence (AI) is having a revolutionary impact on human society. AI and robots assist humans in their daily mental and manual efforts; they augment human intelligence through powerful computing machines and algorithms and replace humans in accomplishing specific tasks, sometimes exceeding human performance.^{1,2} One strategy for developing AI is neuromorphic engineering, which implements neural surrogates through nonbiological systems either for neuroprostheses or to design brain-like computing machines. Traditionally, neural surrogates have been implemented in hardware. Such hardware is rigid if it is made of silicon-based electronic circuits or inorganic memristors. It is flexible if based on organic polymeric films.^{3–7} Quite recently, polyelectrolyte-confined fluidic memristors were also devised.⁸ Alternative neural surrogates in wetware have been implemented through specific fluid nonlinear chemical systems that mimic the dynamics of real neurons.^{9–14} Even hybrid electrochemical devices (with solid electrodes immersed in liquid solution) have been proposed.^{15,16} The principal advantage of working in liquid solutions is the possibility of having information transfer through molecular communication promoted by diffusion, advection, and chemical waves. These processes, along with the unidirectional movement of motor proteins through the cytoskeleton, are also exploited by living beings as basic mechanisms of information transfer at the molecular level.^{17,18}

One of the most common neural surrogates in wetware is the Belousov–Zhabotinsky (BZ) reaction,^{9–14} the metal-

catalyzed oxidative bromination of malonic acid, usually carried out in aqueous solutions. It is a versatile reaction that can reproduce real neurons' oscillatory, excitable, and chaotic regimes. When the BZ reaction is performed in an unstirred thin solution layer, it gives rise to chemical waves.¹⁹ Chemical waves are transient spatiotemporal patterns generated by autocatalytic reactions propagating through an excitable medium.²⁰ When the medium is in an oscillatory regime, three types of chemical waves are usually observable: (1) trigger waves, whose propagation depends on the diffusion of the autocatalytic species, and (2) phase and (3) kinematic waves, which appear to move because of a phase or a frequency gradient, respectively, between oscillating neighboring regions of the solution.²⁰

Like most unstirred nonlinear chemical systems, the BZ reaction is strongly affected by mixing.^{21,22} It therefore seems likely that the chemical waves generated spontaneously in a thin layer of the BZ reaction in a Petri dish might be affected by sound waves and that different acoustic frequencies could induce distinct effects on the BZ spatiotemporal patterns. Sound is a collection of pressure waves (caused by repeated cycles of compression and rarefaction) propagated through

Received: December 27, 2023

Revised: January 3, 2024

Accepted: January 5, 2024

Published: January 29, 2024



elastic media. Frequencies of pressure waves in the 20–20,000 Hz range are typically audible to the human ear.²³

The ear collects sound waves through the outer canal of the auricle. Then, the acoustic waves reach the eardrum, inducing mechanical vibrations. These vibrations are amplified by a system of three ossicle bones behind the tympanic membrane. The last of these three ossicles, the stapes, repeatedly strikes the cochlea's oval window. The cochlea is a spiral-shaped cavity filled with liquid: the mechanical vibrations of the oval window promote the advection of the fluid, which triggers the movement of the basilar membrane. Sound propagates as a traveling wave along the basilar membrane, which is tonotopic because it has heterogeneous structural and mechanical properties. The vibrations of the basilar membrane are transmitted to the organ of Corti, which lies above the membrane and has hair cells.²⁴ The hair cells transform the mechanical energy into electrochemical signals sent to the brain's audible cortex as trains of action potentials. Different frequencies maximally stimulate hair cells above distinct parts of the basilar membrane, resulting in a spatial representation of the sound pitch across the array of hair cells. The array of hair cells above the basilar membrane originates a topographic map of sound frequencies.^{23–25}

In this work, we examine the possibility of using a thin liquid layer of the BZ reaction in a Petri dish subjected to vertical vibrations (see Figure S1 for the experimental setup) as a surrogate for the hair cell array. The vertical oscillations of the Petri dish induce a parametric instability that can generate surface waves called Faraday waves.²⁶ These are standing waves having a frequency (ν_{FW}) equal to one-half the driving frequency (ν_{ex}) when the amplitude of oscillation is below a critical value:^{27,28}

$$\nu_{FW} = \frac{\nu_{ex}}{2} \quad (1)$$

The Faraday waves' frequency and wavelength are linked by the following dispersion relationship, wherein $c = \nu_{FW}\lambda_{FW}$ is the phase speed of the waves:²⁷

$$c^2 = (\nu_{FW}\lambda_{FW})^2 = \left[\frac{g_0\lambda_{FW}}{2\pi} + \frac{\gamma}{\rho} \left(\frac{2\pi}{\lambda_{FW}} \right) \right] \tanh \left(\frac{2\pi}{\lambda_{FW}} h \right) \quad (2)$$

In eq 2, g_0 is the gravitational acceleration, and γ , ρ , and h are the surface tension, density, and thickness of the BZ solution in the Petri dish, respectively.

It is already known that Faraday waves affect the BZ reaction, but previous studies involved a small range of frequencies ($\nu_{ex} \in 7–90$ Hz) and were mainly focused on investigating the effect of vertical vibrational amplitude.^{28,29}

This paper presents new experimental and theoretical analyses of the BZ reaction using an acoustic frequency analyzer. Our system turns out to be sensitive to frequencies between 10 and 2000 Hz. The BZ reaction in the vertically vibrating Petri dish is a transducer of mechanical-into-chemical energy. The periodic spatiotemporal distribution of the mechanical energy delivered by the acoustic waves induces periodic spatiotemporal patterns of mixing in the solution. These mixing patterns affect the local concentrations of all species in the reaction. This mechanical energy is thereby transduced into chemical energy associated with the kinetics (through the free energy of activation, ΔG^\ddagger , which depends on the reagents' and transition states' concentrations) and thermodynamics (through the chemical affinity, A , which

depends on the reagents' and products' concentrations) of the elementary steps characterizing the reaction.

The thin layer of the BZ system is an example of a “liquid computer”³⁰ that maps the periodic input time series related to the acceleration $g(t)$ of the Petri dish:

$$g(t) = Ag_0 \sin(2\pi\nu_{ex}t) \quad (3)$$

onto spatiotemporal chemical patterns as outputs. The features of the emerging patterns allow the discrimination of seven principal bands within the range 10–2000 Hz, as described in the Results section.

METHODS

Experimental Section. Experiments investigating the effects of acoustic frequencies on a thin layer of the BZ reaction were performed using a vibration generator (US6001, 3B Scientific Physics) that consists of a loudspeaker fitted inside a stable plastic housing generating frequencies from 1 to 20,000 Hz and connected to a sinusoidal signal generator and amplifier (IPC) with a maximum power output of 4 W. A mounting pin with a 4 mm socket was attached to the speaker to transmit the oscillations. A circular Petri dish made of polystyrene with an inner diameter of 14 cm was used as the reactor. The cover of the dish was glued to the main dish with a transparent double-face paste to optimize the flatness of the dish. The two glued dishes were clamped to the pin of the vibration generator through a cylindrical holed piece of Plexiglas glued to the central bottom part of the Petri dish. The dish vibrated vertically and synchronously with a pin attached to the speaker. Before each experiment, we checked that the plate was perfectly oriented in a horizontal flat plane. The BZ reaction was carried out in a deionized aqueous solution with a thickness of 2.6 mm. The concentrations of the reagents in the Petri dish were sodium bromate (NaBrO_3), 0.35 M; sulfuric acid (H_2SO_4), 0.35 M; malonic acid ($\text{CH}_2(\text{COOH})_2$), 0.14 M; potassium bromide (KBr), 0.081 M; and ferroin, 1.04 mM. The solution prepared by adding NaBrO_3 , H_2SO_4 , $\text{CH}_2(\text{COOH})_2$, and KBr was first mixed in a beaker until it became transparent (the initial brown color due to bromine disappears when Br_2 reacts and produces bromomalonic acid). Then, ferroin was added, and the system was further mixed for another 5 min before being poured into a Petri dish. After the dish was covered uniformly with the solution, the system was allowed to rest for several minutes, and then specific frequencies of vibration were applied for at least 10 min. The patterns produced by applying different frequencies were recorded through a camera located above the solution (see Figure S1). The videos were processed using homemade software that extracts the values of the three-color coordinates, RGB, from each pixel and every 1 s of the original video. The RGB coordinates vs time data were analyzed with the Origin Professional software. The laboratory temperature was held constant at 22 ± 1 °C, and the thin layer of BZ solution was maintained in physical contact with the air of the laboratory. The response of the BZ reaction was investigated in detail at those acoustic frequencies that resonated with the thin layer of solution in the Petri dish and generated patterns on the surface of the liquid. The chemical response at each acoustic frequency was investigated at least twice in independent experiments and for solutions with a different degree of aging. The qualitative features of the spatiotemporal patterns are

reproducible, and their quantitative features are obtained as averages of two or more distinct experiments.

Computational Details. The “networks-of-zones” model²¹ was applied in this work to interpret the dependence of the advection-induced phase waves’ (AIPWs) velocity on the acoustic frequency. We considered a square Petri dish of 100×100 units of space (u.s.) partitioned into a collection of $n_s \times n_s = 200 \times 200$ cells, each assumed to have an internal homogeneous chemical environment and be exchanging molecules with the adjacent cells. Whenever an acoustic frequency is applied to the solution in the Petri dish, Faraday waves emerge. The Faraday patterns, which depend on the applied acoustic frequency, induce aggregation of the cells due to the advection of the fluid. The linear dimensions of the aggregates or clusters of cells coincide with the Faraday waves’ wavelength (λ_{FW}). The wavelength and frequency of the Faraday waves are related by eq 2. For our system, $\gamma = 60.9$ mN/m is the surface tension of the BZ solution,²⁸ $g = 9.8$ m/s² is the gravitational acceleration, $\rho = 1067$ kg/m³ is the liquid density,²⁸ and $h = 0.0026$ m is the thickness of the solution in the Petri dish. Figure S2A shows the dependence of the Faraday waves’ wavelength (λ_{FW}) on the vibrational driving frequency (ν_{ex}). In the frequency interval 10–2000 Hz, λ_{FW} ranges from 3.3 cm to 700 μ m. The number of clusters (N) can be estimated through the following equation: $N = A/A_c$, where $A = \pi R^2$ is the area of the system, $A_c = \pi r^2$ is the area of the cluster of cells, and $r = \lambda_{FW}/2$ by assumption. Therefore, the number (N) of clusters within the Petri dish is

$$N = \frac{4R^2}{(\lambda_{FW})^2} \quad (4)$$

where $R = 7$ cm is the radius of the Petri dish. The value of N grows from about 25 for $\nu_{ex} = 10$ Hz to about 40,000, i.e., the total number of cells, for $\nu_{ex} = 2000$ Hz, as shown in Figure S2B. When $\nu_{ex} = 2000$ Hz, each cluster consists of just one cell. From this analysis, we can correlate the seven frequency bands explored in the experimental section with the number of clusters of cells formed in the surface of the fluid:

First band(650 – 2000)Hz: $N \in (8619 - 40,000)$

Second band(500 – 650)Hz: $N \in (6058 - 8619)$

Third band(200 – 500)Hz: $N \in (1746 - 6058)$

Fourth band(95 – 200)Hz: $N \in (615 - 1746)$

Fifth band(50 – 95)Hz: $N \in (240 - 615)$

Sixth band(15 – 50)Hz: $N \in (35 - 240)$

Seventh band(10 – 15)Hz: $N \in (17 - 35)$

Figure S3 shows, as an example, the effect of an acoustic frequency of $\nu_{ex} \approx 10$ Hz on the aggregation of the cells: the theoretical square Petri dish is partitioned into $N = n_c \times n_c = 5 \times 5 = 25$ clusters of cells, with each cluster consisting of $(n_s/n_c) \times (n_s/n_c) = (200/5) \times (200/5) = 40 \times 40$ single cells. If l represents the linear dimension of a single cell, then $\lambda_{FW} = \left(\frac{n_s}{n_c}\right)l$.

A realistic model of the BZ reaction for describing the formation of chemical waves is that proposed by Tyson and Fife,³¹ who started from the Oregonator model and rearranged it into a system of two differential equations having the

concentrations of HBrO_2 (u) and Ce^{4+} (v) as the two variables. The concentration of the other major species of the Oregonator model, i.e., Br^- , changes on the fastest time scale, and its value is determined by the instantaneous values of u and v . The system of two differential equations for the cell indexed as (i, j) , with $1 \leq i, j \leq n_s$, is

$$\frac{du_{i,j}}{dt} = \left[u_{i,j} \left(1 - u_{i,j} \right) - fv_{i,j} \frac{(u_{i,j} - a)}{(u_{i,j} + a)} \right] \frac{1}{\varepsilon} \quad (5a)$$

$$\frac{dv_{i,j}}{dt} = u_{i,j} - v_{i,j} \quad (5b)$$

In eq 5a, ε and a are parameters that depend on the initial concentrations of the reagents and the rate constants of some elementary steps of the Oregonator;³¹ f is a stoichiometric factor equal to $-2(d[\text{Br}^-]/d[\text{Ce}^{4+}])$.³¹

The cell indexed as (i, j) exchanges reagents with the surrounding cells. The mass exchange can be accounted for in eqs 5a and 5b by introducing two new terms: $\sum_{(n, m)} k_c (u_{n, m} - u_{i, j})$ and $\sum_{(n, m)} k_c (v_{n, m} - v_{i, j})$, respectively. The summations are over the neighboring cells of (i, j) . The number of neighboring cells depends on λ_{FW} . More specifically,

$$(n, m) := \{(n, m) \in n_s \times n_s | (n - i)^2 + (m - j)^2 \leq \left(\frac{n_s}{n_c}\right)^2, n \neq i, m \neq j\} \quad (6)$$

Figure S3B depicts a green circle enclosing the neighborhood of a generic (i, j) cell for the case of $n_c = 5$.

The terms proportional to k_c take into account the effect of the Faraday waves that generate cellular clusters delimited by the nodal regions of the waves. The matter exchange is maximal in the antinodal regions and minimal in the nodal regions of the waves. Therefore, we express k_c as

$$k_c = \alpha + \beta \left(1 - \frac{n_c}{n_s} \right) \sin\left(\frac{x\pi}{\lambda_{FW}}\right) \sin\left(\frac{y\pi}{\lambda_{FW}}\right) \\ = \alpha + \beta \left(1 - \frac{n_c}{n_s} \right) \sin\left(\frac{\frac{x\pi}{n_s} l}{\frac{n_s}{n_c} l}\right) \sin\left(\frac{\frac{y\pi}{n_s} l}{\frac{n_s}{n_c} l}\right) \quad (7)$$

In eq 7, x and y are the two spatial coordinates, whereas α and β are constants that characterize the effectiveness of mass exchange. The profile of $\alpha + \beta \left(1 - \frac{n_c}{n_s} \right)$ vs n_c is shown in Figure S4 for $\alpha = 0.1$ and $\beta = 10$. These values for α and β have been chosen to reproduce the dependence of the AIPWs’ velocity on the acoustic frequency. In particular, the value of α was fixed to ensure the formation of chemical waves even when acoustic frequencies of the order of 2000 Hz were applied (i.e., when $n_c = n_s$). On the other hand, β was fixed to represent the effect of advection, which is particularly pronounced at lower acoustic frequencies.

Figure S5 depicts k_c in the (x, y) plane for $n_c = 5$, i.e., $\nu_{ex} \approx 10$ Hz. k_c ranges between 10 in the center of the antinodal region and 0.1 along the nodes of the waves. Finally, because k_c must describe the effect of advection for cells belonging to the same cluster and must wane for those that are far apart, we introduce the effect of distance through the following definition:

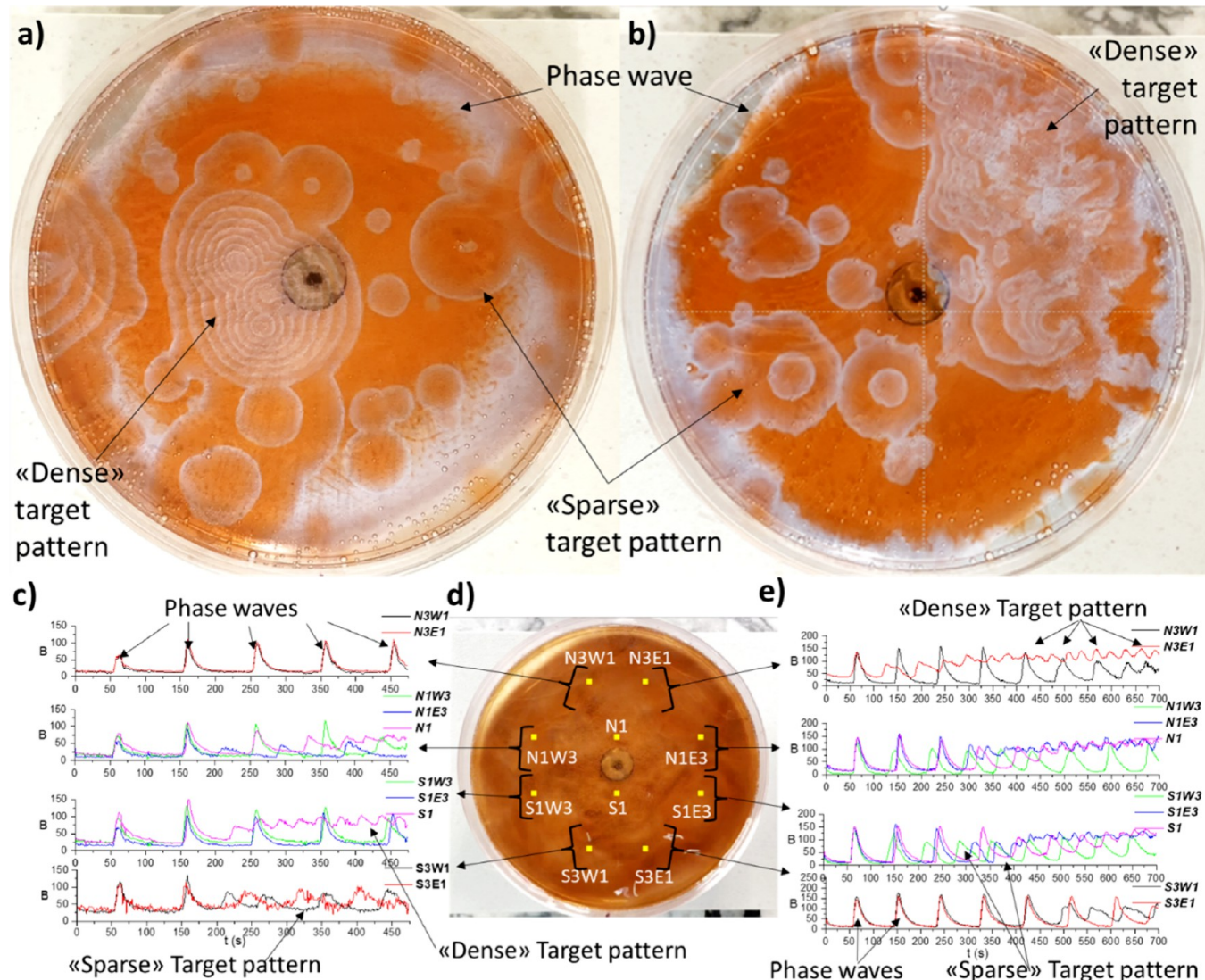


Figure 1. Types of chemical waves detectable for an unperturbed thin layer of the BZ reaction in panel a and when an acoustic frequency of 680 Hz is applied in panel b. Graphs in panel c show the time evolution of the color coordinate B for the unperturbed BZ solution at the yellow points labeled in panel d. (e) Time evolution of B at the same highlighted points but at an acoustic frequency of 680 Hz.

$$K_c = \frac{k_c}{\|r\|}, \|r\| = l[(n - i)^2 + (m - j)^2]^{1/2} \quad (8)$$

The final version of the two differential equations that describe the behavior of the BZ reaction in the presence of Faraday waves is

$$\frac{du_{i,j}}{dt} = \left[u_{i,j} (1 - u_{i,j}) - fv_{i,j} \frac{(u_{i,j} - a)}{(u_{i,j} + a)} \right] \frac{1}{\varepsilon} + \sum_{\langle n,m \rangle} K_c (u_{n,m} - u_{i,j}) \quad (9a)$$

$$\frac{dv_{i,j}}{dt} = u_{i,j} - v_{i,j} + \sum_{\langle n,m \rangle} K_c (v_{n,m} - v_{i,j}) \quad (9b)$$

with $i, j = 1, 2, \dots, n_s$.

The differential eqs 9a and 9b were numerically solved using the adaptive fourth–fifth-order Runge–Kutta–Fehlberg method, which was implemented in Fortran. The simulations utilize a 100×100 unit space system with solid walls and composed

of 200×200 cells. The space unit corresponds to the linear dimension of two elementary cells, which is $0.07 \text{ cm} \times 2 = 0.14 \text{ cm}$. The time unit is $t = (k_s B_M) \cdot \text{time} = (0.5 \text{ s}^{-1}) \cdot \text{time}$, where k_s is the kinetic constant of the last elementary step of the Oregonator and B_M represents the concentration of malonic and bromomalonic acids. The kinetic parameters $a = 0.002$ and $\varepsilon = 0.01$ were fixed. The value of f was variable. Because the purpose of the simulations was to determine the chemical waves' velocity as a function of the acoustic frequency ν_{ex} , the value of f was set to 2.0 for $x \leq 1$ and to 2.7 elsewhere. Under the latter condition, the BZ reaction is in its excitable regime, whereas for the former condition, it is in its oscillatory regime.

RESULTS

An unperturbed thin layer of BZ reaction gives rise to (1) phase waves (PW) originating at the periphery of the dish and moving toward its center and (2) target patterns (TP), which can be dense (D) or sparse (S) and form in different and unpredictable regions of the dish (see Figure 1a and the 10-times-accelerated Video E0 in the Supporting Information).

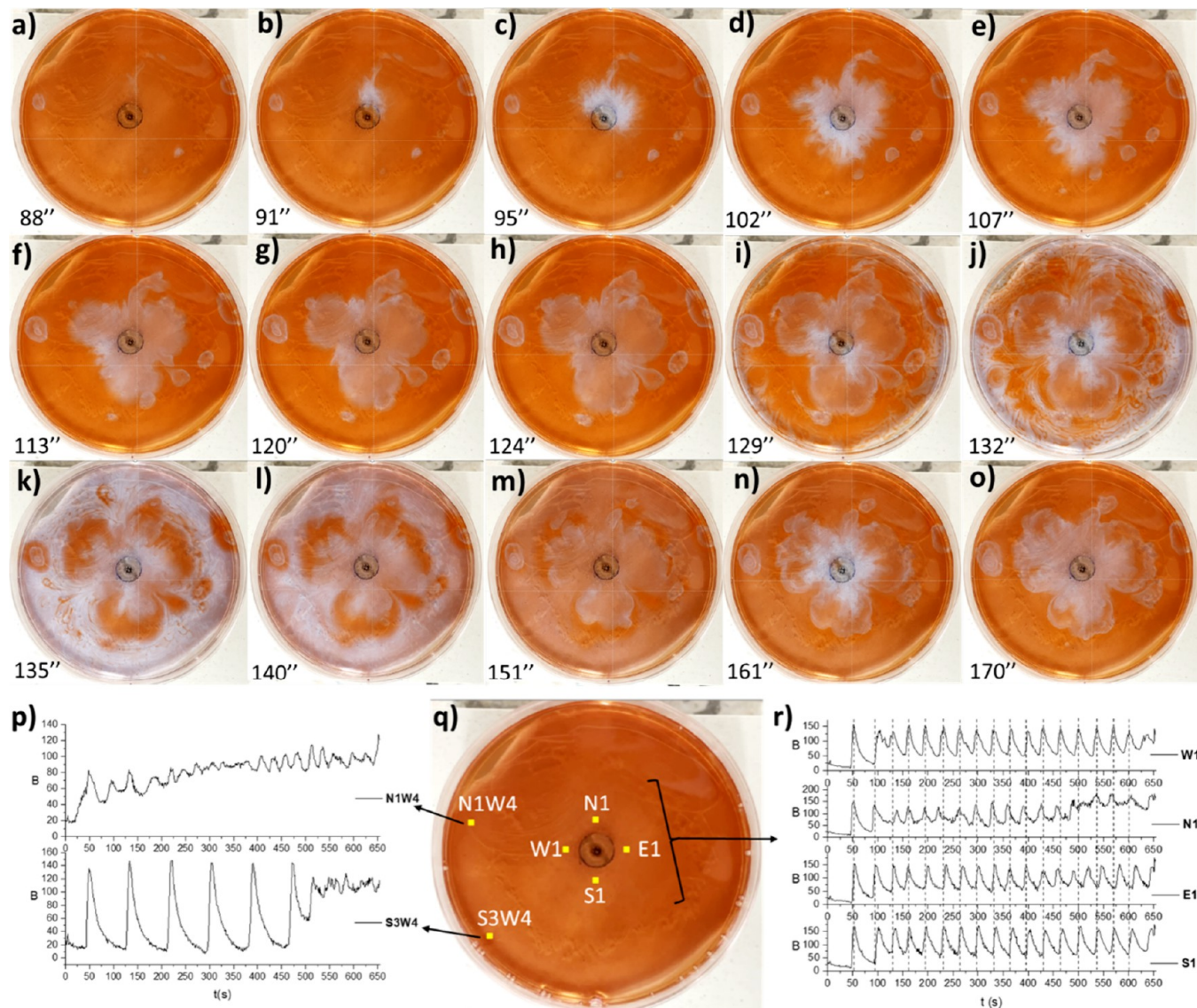


Figure 2. Snapshots a–o (taken at the times indicated in seconds at the bottom left of each frame) show the typical evolution of spatiotemporal patterns generated by the BZ reaction when it responds to an acoustic frequency of 634 Hz. Graphs p and r show B vs time for the yellow points highlighted in q.

The phase waves have a frequency of $\nu_{PW} = (1/98) = 0.010\text{s}^{-1}$ (see Figure 1c), which is less than half of the frequency of oscillation ($\nu_{Osc} = (1/45) = 0.022\text{s}^{-1}$) for the same BZ reaction carried out under magnetic stirring within a beaker. The velocity of the phase waves decreases as the solution ages. The phase waves are annihilated when they collide with the target patterns. The pacemaker central point of any target pattern generates circular fronts with a higher frequency than the bulk solution: $\nu_{STP} = (1/89 \pm 4) = (0.0112 \pm 0.0005)\text{s}^{-1}$ for sparse target patterns (see Figure 1c) and $\nu_{DTP} = (1/29.25 \pm 1.25) = (0.0340 \pm 0.0015)\text{s}^{-1}$ for dense target patterns (see Figure 1c). The regions of the solution where target patterns emerge desynchronize with respect to the rest of the solution (Figure S6 in the SI). The target patterns propagate with a velocity of $\bar{v}_{TP} = 0.0110 \pm 0.0006 \text{ cm/s}$. Therefore, the wavelengths are $\lambda_{STP} = (\bar{v}/\nu_{STP}) = (0.982 \pm 0.097)\text{cm}$ and $\lambda_{DTP} = (\bar{v}/\nu_{DTP}) = (0.32 \pm 0.03)\text{cm}$ for the sparse and dense target patterns, respectively.

First Band: 650–2000 Hz. Acoustic frequencies below 2000 Hz affect the spatiotemporal patterns generated spontaneously by the reaction. Phase waves and target patterns are still observable. However, the target patterns lose their characteristic circular shape and become more irregular than those of the unperturbed BZ reaction (see Figure 1b, Figure S7, and Video E1, which shows the 10-times-accelerated response to $\nu_{ex} = 680$ Hz). The phase waves originate at the periphery of the dish with an average frequency of $\nu_{PW} \approx (1/95) = 0.0105\text{s}^{-1}$ (Figure 1e), and they move toward its center with a velocity that diminishes on aging because the phase gradient increases with time. The phase waves are annihilated whenever they collide with target patterns. The target patterns emerge unpredictably in different parts of the solution with an average frequency of $\nu_{STP} \approx (1/65) = 0.015\text{s}^{-1}$ and $\nu_{DTP} \approx (1/30) = 0.033\text{s}^{-1}$ for sparse and dense patterns,

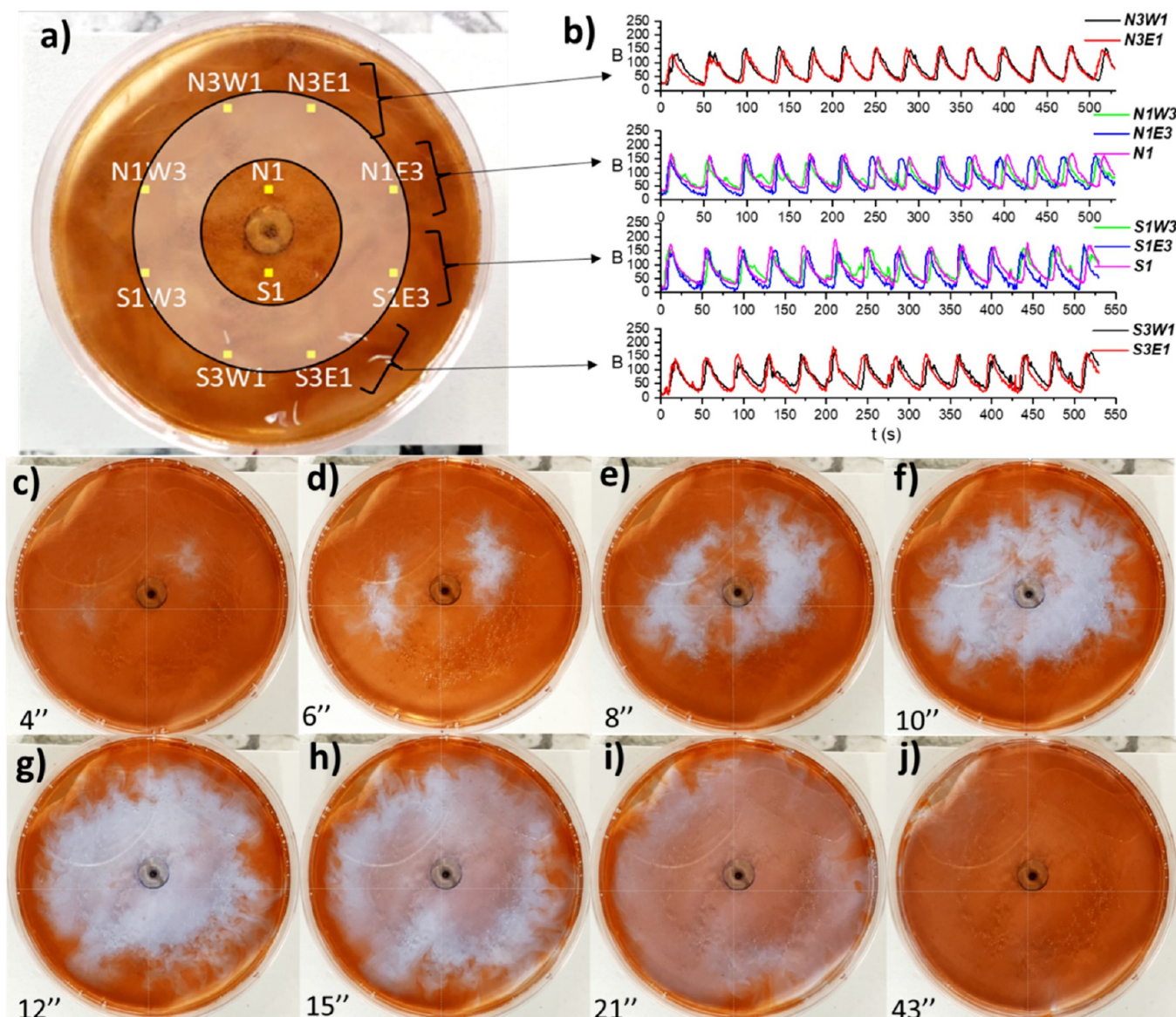


Figure 3. Partially transparent annulus depicted within the thin layer of the BZ reaction in panel a represents the region in which the solution vibrates when frequencies within the third band are applied (the width of the annulus depends on the applied frequency). Time series of B extracted from the yellow points in panel a are reported in panel b for $\nu_{ex} = 390$ Hz. The sequence of snapshots c–j (taken at the times indicated in seconds at the lower left of each frame measured from the moment of applying the acoustic frequency) shows the evolution of the spatiotemporal pattern generated by an acoustic frequency of 390 Hz.

respectively (see Figure 1e). Their front waves propagate with a velocity of roughly $\bar{v}_{TP} \approx 0.01$ cm/s. The wavelength of the sparse targets is $\lambda_{STP} = (\bar{v}/\nu)_{STP} \approx 0.65$ cm, whereas that of the dense patterns is difficult to determine because the fronts are wavy and the patterns are not concentric. Whenever a target pattern is formed, that portion of the solution desynchronizes from the rest (Figure S8).

Second Band: 500–650 Hz. Below 650 Hz, the acoustic frequencies exert more pronounced effects. When the acoustic frequency is between 500 and 650 Hz, a pacemaker of plumes arises in the center of the dish. It generates advection-induced phase waves (AIPWs) with an average frequency of $\nu_{AIPW} \cong (1/30) = 0.033$ s⁻¹. They propagate toward the periphery of the dish with a velocity of $\bar{v}_{AIPW} \cong 0.3$ cm/s, giving rise to “clover-type” shapes (see snapshots a–o in Figure 2 and the 10-times-accelerated Video E2 in the Supporting Information).

The periphery of the Petri dish is still a source of spontaneous phase waves such as those observed in the unperturbed system and in response to the acoustic frequencies of the first band. These peripheral phase waves are generated with an average frequency of $\nu_{PW} \approx (1/84) = 0.012$ s⁻¹ (see the plot of B vs time for point S3W4 in Figure 2p), and they move toward the center of the dish, opposite to the direction of motion of the previously described AIPWs. As usual, their velocity appreciably decreases as the solution ages. When the two types of phase waves (AIPW and spontaneous PW) collide, they annihilate. In the periphery of the dish, dense target patterns also form (see snapshots f–o in Figure 2). Their formation frequency is $\nu_{DTP} \approx (1/25) = 0.04$ s⁻¹, and they propagate with a velocity $\bar{v}_{TP} \approx 0.02$ cm/s. The central points of the solution are highly synchronized (see Figure 2r), whereas they are poorly correlated with the peripheral points due to the distinct

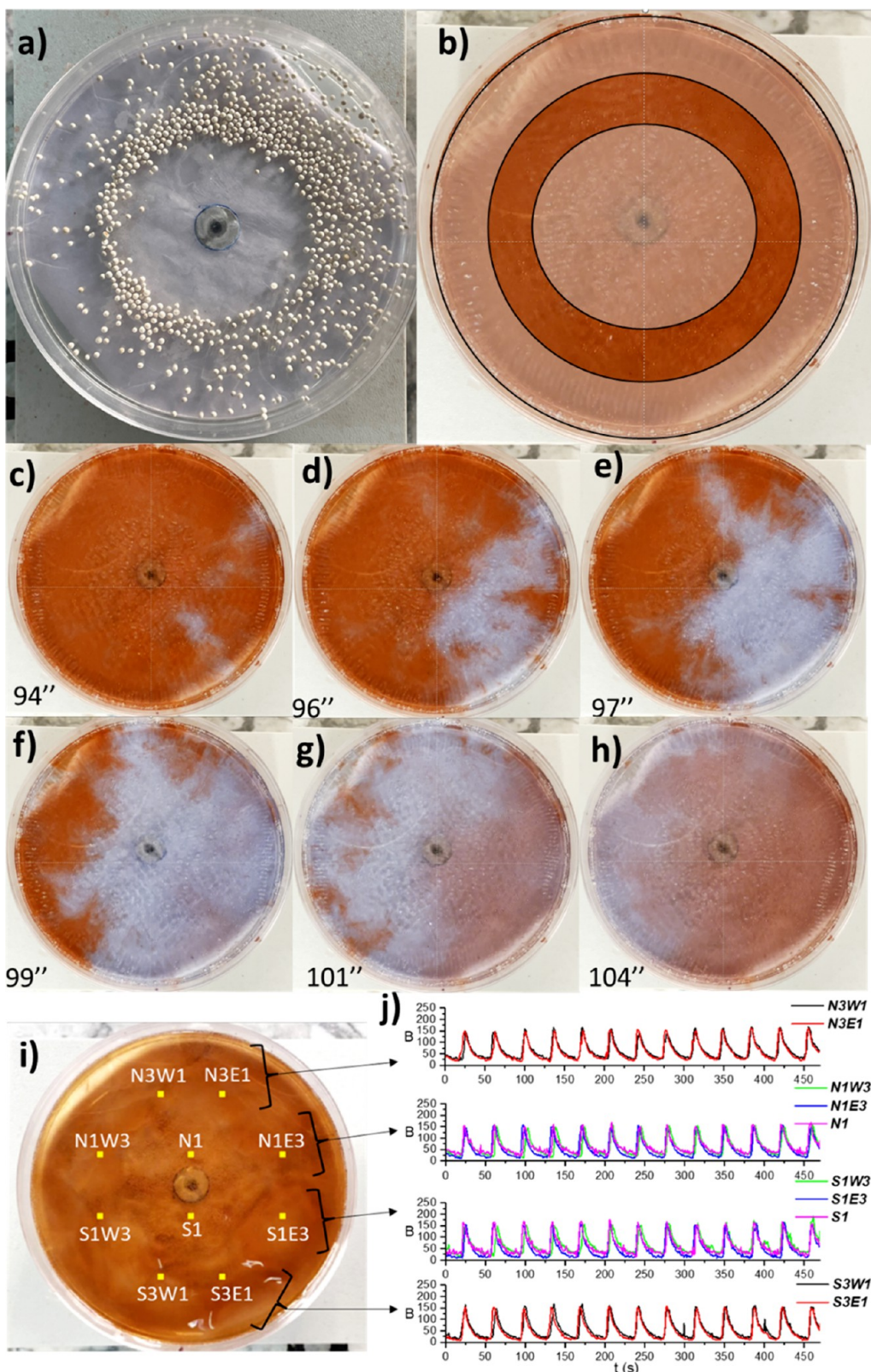


Figure 4. (a) The nodal region occupied by molecular sieves when $\nu_{\text{ex}} = 130$ Hz. In panel b, the central and peripheral antinodes, where the solution visibly vibrates, lie within a partially transparent circle and annulus, respectively. The sequence of snapshots c–h reveals the evolution of the spatiotemporal patterns that emerge when $\nu_{\text{ex}} = 130$ Hz. (j) Evolution of B for the yellow points highlighted in panel i.

spatiotemporal patterns emerging in these two parts of the dish ([Figure S9](#)). The responses of the reaction to other frequencies included in this second band are shown in [Figures S10–S12](#) of the SI. The remarkably different behavior between the central

and peripheral regions of the solution results from the presence of a peripheral nodal region, as evidenced by the pattern visualized with spherical molecular sieves free to slide on the vibrating Petri dish (see [Figure S13](#)).

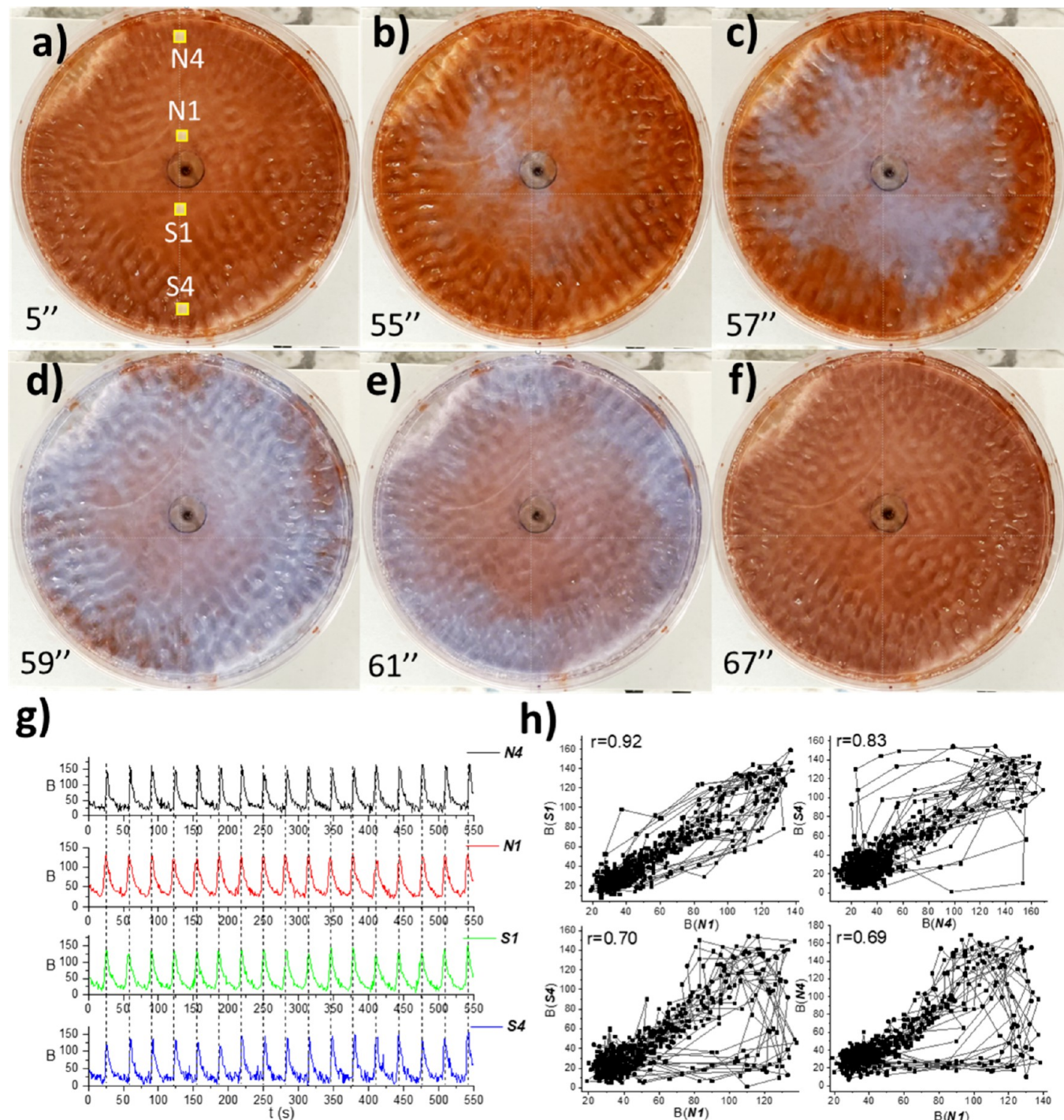


Figure 5. (a–f) Typical time evolution of advection-induced phase waves that originate when acoustic frequencies belonging to the fifth band (i.e., $\nu_{\text{ex}}\epsilon$ (50–95) Hz) are applied. (g) Kinetics of B for the four yellow points shown in panel a. (h) Correlation between N1 and S1 (top left), N1 and S4 (bottom left), N4 and S4 (top right), and N1 and N4 (bottom right).

Third Band: 200–500 Hz. When the BZ reaction is subjected to vertical vibrations of frequency 200–500 Hz, an annular portion of its surface, depicted in Figure 3a, undergoes a macroscopic vibration. These localized vibrations affect the behavior of the reaction. The color transition from red to blue always starts within the vibrating annulus (Figure 3c,d). Convective-like plumes propagate, at first toward the center of the dish (Figure 3e,f) and then toward the periphery (Figure 3g,h). Finally, the original red state is recovered everywhere, as shown in Figure 3i,j. The advection-induced phase waves

generated within the annulus have rough labyrinthine interfaces and propagate anisotropically, i.e., with different velocities depending on the direction of the propagation, reaching a maximum of $\bar{v}_{\text{AIPW}} \approx 0.5$ cm/s. Their average frequency of appearance is $\nu_{\text{AIPW}} = (1/(34 \pm 1)) = (0.029 \pm 0.001)\text{s}^{-1}$. Points within the vibrating annulus and those included in its interior show a high degree of synchronization, as demonstrated by the plots of B vs time in Figure 3b and the values of the correlation coefficients,

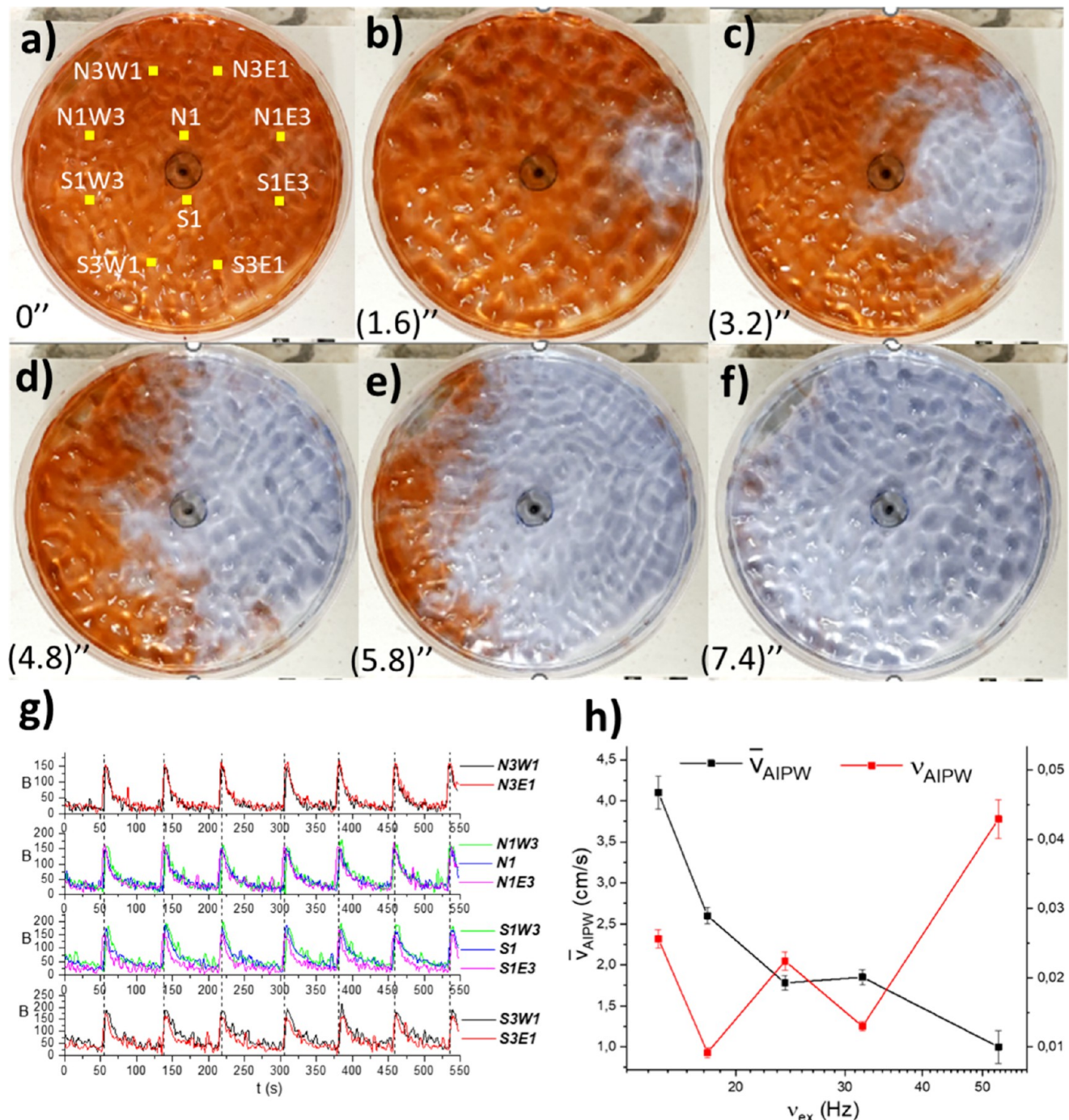


Figure 6. (a–f) Typical spatiotemporal pattern when acoustic frequencies in the sixth band (15–50 Hz) are applied. (g) Temporal evolution of B for the yellow points marked in panel a, recorded with $\nu_{\text{ex}} = 32$ Hz. (h) Average velocity of advection-induced phase waves \bar{v}_{AIPW} and frequency $\nu_{\text{AIPW}} = (1/\bar{T}_{\text{AIPW}})$ of their formation as functions of the applied acoustic frequency (ν_{ex}) within the sixth band.

which are, in general, $r > 0.50$ (see Figure S14). On the other hand, the peripheral points are less synchronized with the central points of the dish as demonstrated by their lower correlation coefficients, which are generally $r \leq 0.50$ (see Figure S14). Video E3 shows the 10-times-accelerated behavior of the reaction when an acoustic frequency of 390 Hz is applied. The responses to other frequencies included in the third band are shown in Figures S15–S17 of the SI.

Fourth Band: 95–200 Hz. In the fourth band, we observe two vibrating regions: a circular area in the central part of the dish and an annulus in the periphery (Figure 4b), separated by

a steady nodal region, as confirmed by the molecular sieves in Figure 4a. The color transition from red to blue starts at random points within the two vibrating antinodes (Figure 4c), usually from one side of the peripheral antinode. Then, the blue color spreads swiftly in the neighborhood, engulfing the central antinode (Figure 4d,e). Finally, these advection-induced phase waves propagate, with an average velocity $\bar{v}_{\text{AIPW}} \cong 1$ cm/s and irregular fronts, toward the opposite side of the dish from where they originally emerge (Figure 4f–h). The AIPWs are generated with an average frequency of $\nu_{\text{AIPW}} = (1/(35 \pm 1)) = (0.028 \pm 0.001)\text{s}^{-1}$ as shown in Figure

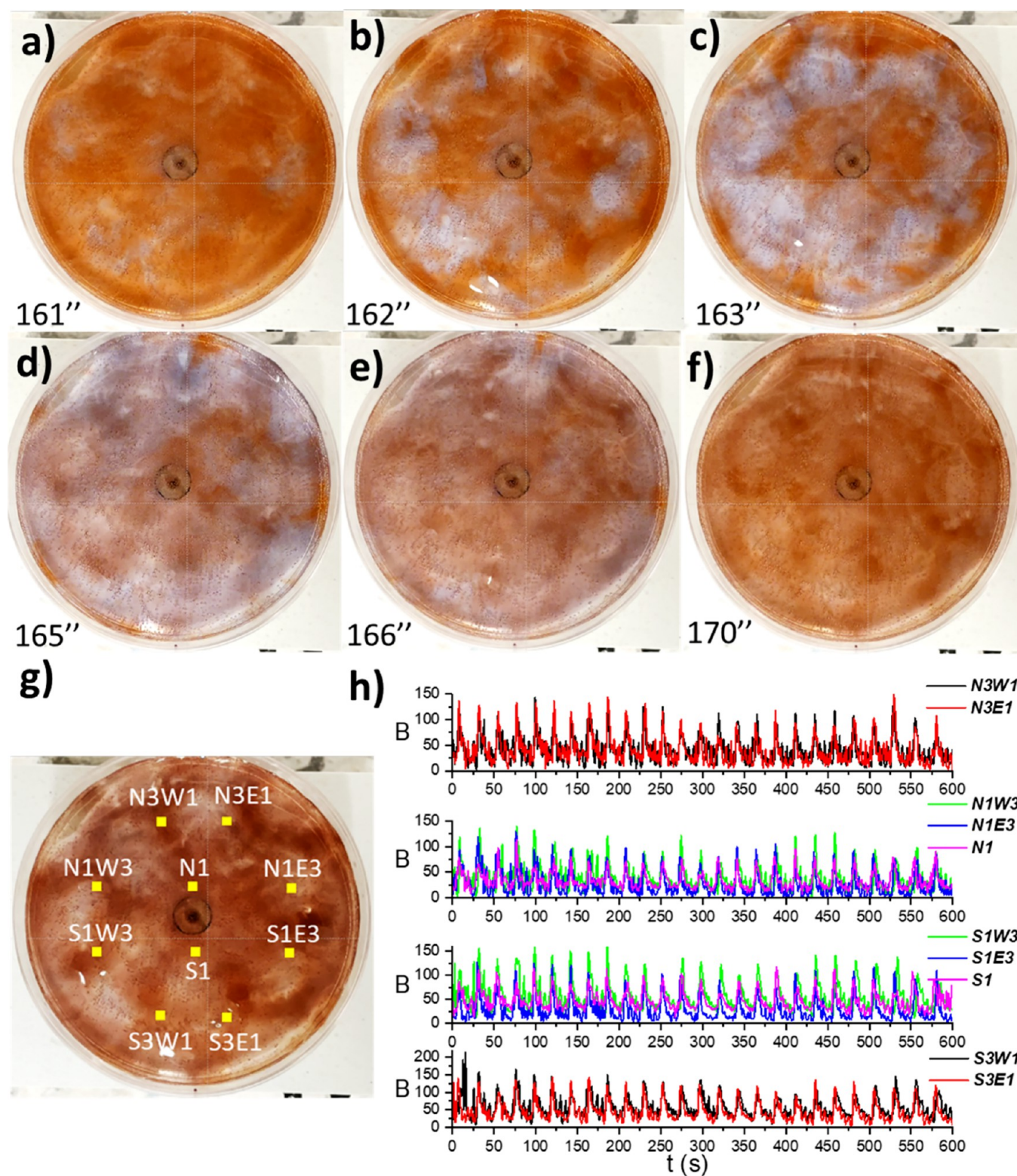


Figure 7. (a–f) Typical spatiotemporal pattern of the seventh band. (h) Time evolution of B for the yellow points highlighted in (g).

4j, which depicts the behavior of B vs time for the points highlighted in Figure 4i. The kinetics reported in Figure 4j are significantly overlapped, demonstrating the high degree of synchronization between the different portions of the solution, as quantitatively confirmed by the large positive correlation coefficients (Figure S18 in the SI). Neighboring points belonging to the two distinct antinodes, shown in Figure 4b,

exhibit a high correlation coefficient ($r = 0.92$); i.e., they are almost exactly in phase. Distant points belonging to opposite sides of the dish are less correlated ($0.73 \leq r \leq 0.78$) and slightly out-of-phase. Video E4 in the SI shows the 10-times-accelerated response of the BZ reaction when the acoustic frequency $\nu_{\text{ex}} = 130$ Hz is applied. Responses to other

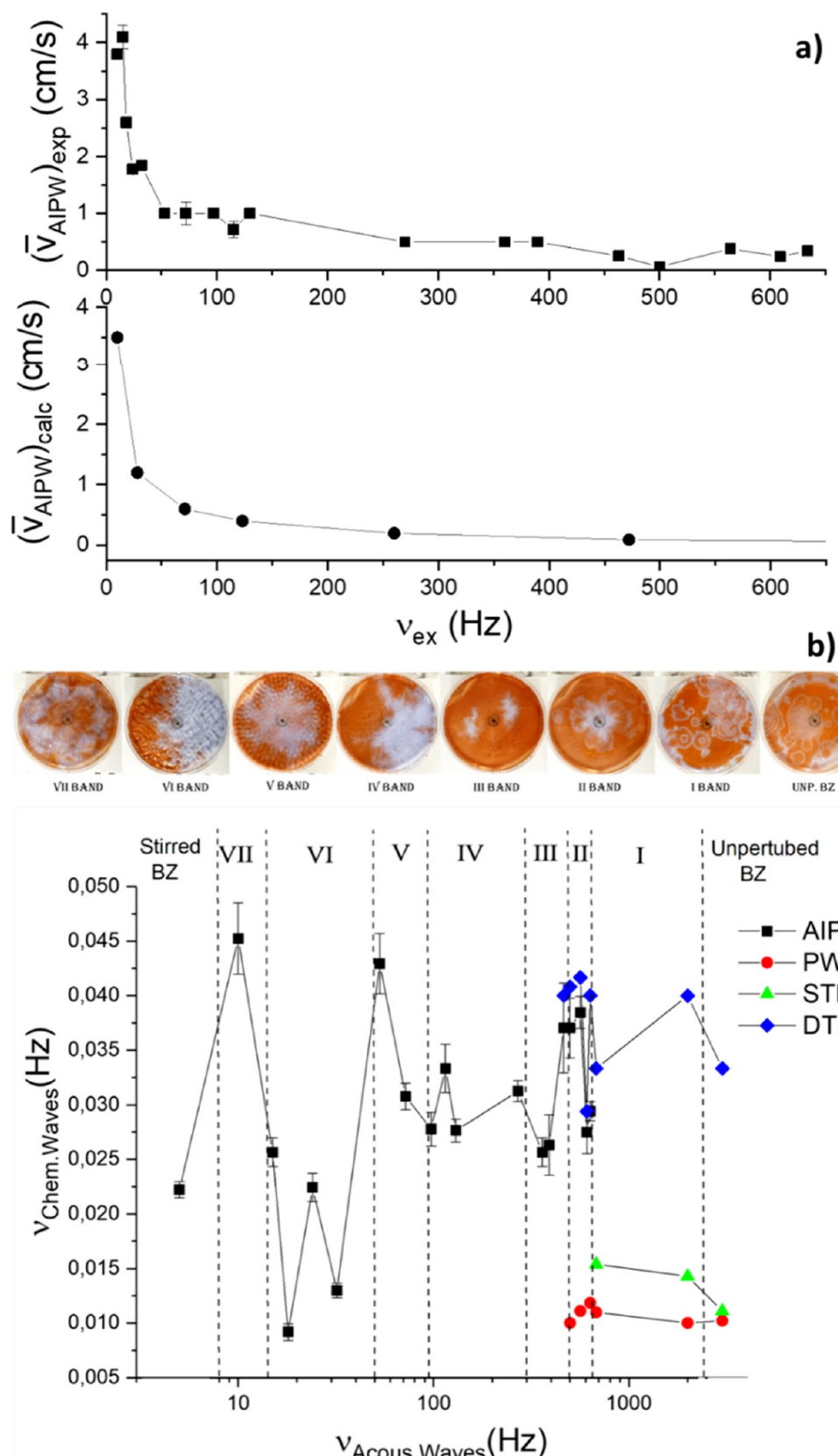


Figure 8. (a) Dependence of AIPW velocity on the acoustic frequency (ν_{ex}) in experiments (top panel) and simulations (lower panel). (b) Dependence of the frequency of spatiotemporal chemical patterns in the BZ reaction on the acoustic frequency, partitioned in bands according to the patterns found experimentally.

frequencies in the fourth band (i.e., 95–200 Hz) are shown in Figures S19 and S20 of the SI.

Fifth Band: 50–95 Hz. The acoustic frequencies of the fifth band generate Faraday wave patterns characterized by two

distinct regions: one in the periphery of the dish with deep troughs and high crests and the other in the center, where the surface of the solution appears much flatter (see Figure 5a and the 10-times-accelerated Video E5 recorded at an acoustic frequency of 72 Hz). The color transition from red to blue is triggered within the central region (Figure 5b). Then, it sweeps the entire central portion of the solution (Figure 5c). Finally, the advection-induced phase wave, with irregular fronts (see Figure 5d,e), propagates toward the periphery at a velocity of $\bar{v}_{\text{AIPW}} \cong 1 \text{ cm/s}$. Hence, the original red state is recovered in the whole solution (Figure 5f). This cycle of events, involving all the points in the dish, repeats with an average frequency $\nu_{\text{AIPW}} = (1/(33 \pm 1)) = (0.030 \pm 0.001)\text{s}^{-1}$ when $\nu_{\text{ex}} = 72 \text{ Hz}$ (Figure 5g). The points of the central region oscillate almost-in-phase, as shown for the pair N1 and S1 (red and green traces in Figure 5g), which has an average phase difference of $\Delta\varphi = 1^\circ$ and a correlation coefficient of $r = 0.92$ (see the top-left graph of Figure 5h). The peripheral points are also almost in-phase as shown for the pair N4 and S4 (see the black and blue kinetics in Figure 5g), which has a correlation coefficient of $r = 0.83$ (see the top-right graph of Figure 5h). The phase difference becomes larger if the behaviors of peripheral and central points are compared. For instance, the central point N1 is out-of-phase (with $\Delta\varphi \cong 20^\circ$) with respect to the peripheral points N4 and S4 and is less correlated with them ($r \leq 0.70$, see the bottom graphs of Figure 5h) than with the central S1. Analogous synchronization conditions are established among the points of the BZ solution when other acoustic frequencies in the fifth band are applied, as shown, for example, for $\nu_{\text{ex}} = 53 \text{ Hz}$ in Figure S21.

Sixth Band: 15–50 Hz. Acoustic frequencies in the sixth band give rise to Faraday patterns, which appear as grids of cells uniformly distributed across the solution. The lower the frequency is, the larger are the cells (see eq 2 above). In all experiments with acoustic frequencies in this band, the spatiotemporal pattern resembles that shown in the sequence of snapshots a–f of Figure 6 and also in Figures S22–S24. The red-to-blue color transition starts at the periphery of the dish and then quickly propagates toward the opposite side of the dish, sweeping the entire solution. The front waves appear as rough labyrinthine interfaces. The site where the advection-induced phase waves originate varies randomly, even within the same experiment, as seen in Video E6 of the SI, which shows the 10-times-accelerated response to an acoustic frequency of $\nu_{\text{ex}} = 32 \text{ Hz}$.

A peculiarity of this sixth band is the noticeable changes in the advection-induced phase wave velocity (\bar{v}_{AIPW}) and formation frequency ($\nu_{\text{AIPW}} = (1/T_{\text{AIPW}})$) with the acoustic frequency (ν_{ex}), as depicted in Figure 6h. The velocity increases four times from about 1 cm/s when $\nu_{\text{ex}} \approx 50 \text{ Hz}$ to 4 cm/s when $\nu_{\text{ex}} = 15 \text{ Hz}$. On the other hand, the frequency ν_{AIPW} exhibits a sawtooth profile: for $\nu_{\text{ex}} = 24$ and 15 Hz, the frequencies of the AIPW formation ($\nu_{\text{AIPW}} \approx 0.022 \text{ s}^{-1}$) are comparable to the characteristic frequency of color change for the BZ reaction with the same reagent concentrations under magnetic stirring in a beaker ($\nu_{\text{osc}} \cong 0.022 \text{ s}^{-1}$). When $\nu_{\text{ex}} = 32$ and 18 Hz, ν_{AIPW} is about half as large: 0.013 and 0.009 s⁻¹, respectively. On the other hand, when $\nu_{\text{ex}} \approx 50 \text{ Hz}$, ν_{AIPW} roughly doubles to $\approx 0.04 \text{ s}^{-1}$. This curious trend cannot be attributed to the amplitudes of the mechanical vibrations, which are of the order of $2g_0$, where g_0 is the acceleration of gravity (see eq 3 above), when $\nu_{\text{ex}} \approx 50, 32, \text{ and } 24 \text{ Hz}$; $1.2g_0$

when $\nu_{\text{ex}} = 18 \text{ Hz}$; and $0.5g_0$ when $\nu_{\text{ex}} = 15 \text{ Hz}$ (see Figure S25). The dependence of ν_{AIPW} on ν_{ex} within this sixth band will be a matter for future investigation.

Seventh Band: 10–15 Hz. At low frequencies, the Faraday patterns are characterized by cells with linear dimensions of a few centimeters (see Figure 7g, where the crests of the cells appear bright red and are surrounded by dark red troughs). These large sizes affect the formation and propagation of the advection-induced phase waves. As shown by the sequence of snapshots a–f in Figure 7, the color transition from red to blue occurs in different parts of the solution, irregularly distributed within the Petri dish. Then, the blue color propagates anisotropically, and the AIPWs appear fragmented. Their velocity \bar{v}_{AIPW} reaches values as high as 3.8 cm/s in the preferred direction of motion. The generation of the AIPWs repeats with a frequency $\nu_{\text{AIPW}} = (1/(22 \pm 2)) = (0.045 \pm 0.004)\text{s}^{-1}$ everywhere in the solution, as shown by the temporal evolution of B in Figure 7h. Video E7 reports the 10-times-accelerated response of the system to an acoustic frequency $\nu_{\text{ex}} = 10 \text{ Hz}$.

Theoretical Model. The experimental results described above demonstrate that vertical mechanical vibrations having frequencies in the acoustic range 10–2000 Hz affect the behavior of the BZ reaction because an inhomogeneous distribution of the reagents gives rise to a heterogeneous dynamical behavior. Typically, two levels of mixing may be distinguished: (1) “micromixing”, occurring at the molecular level and promoted by diffusion, and (2) “macromixing”, related to the hydrodynamic features of the solution, governed by advection.³² The effects of inhomogeneous macromixing in a solution can be interpreted by invoking the “networks-of-zones” model (also called the global fluid flow field model).²¹ This model partitions the macroscopic solution into an array of zones or cells, each perfectly mixed and exchanging material with adjacent cells as if it were a continuous-flow stirred tank reactor (CSTR). Each cell has a rectangular parallelepiped shape, whose height coincides with the depth of the solution, and a square base 700 μm on a side. Acoustic frequencies from 10 to 2000 Hz induce the aggregation of adjacent cells through advection. The linear dimensions of the emerging cellular clusters depend on the Faraday wavelength (see eq 2 and the computational section for more details) and hence the acoustic frequency. When $\nu_{\text{ex}} \approx 2000 \text{ Hz}$, $\lambda_{\text{FW}} \approx 700 \mu\text{m}$, and single cells do not aggregate. When $\nu_{\text{ex}} \approx 10 \text{ Hz}$, $\lambda_{\text{FW}} \approx 2.8 \text{ cm}$, and clusters consisting of 40×40 single cells form. The lower acoustic frequencies produce larger clusters and, hence, a more extended chemical coupling. We combine the “networks-of-zones” model with the Oregonator for the mechanistic aspects of the BZ reaction³¹ to interpret the dependence of the AIPWs’ velocity on the acoustic frequency (the details of the simulations are described in the computational section). The results are shown in Figure 8a and Figure S26. The simulated dependence of \bar{v}_{AIPW} on ν_{ex} reproduces the experimental monotonic trend and yields quantitative results in good agreement with the experimental data (see also Table S1): when $\nu_{\text{ex}} < 50 \text{ Hz}$, the cellular clusters have linear dimensions $\geq 1 \text{ cm}$, and the AIPWs’ velocity (\bar{v}_{AIPW}) is $\geq 1 \text{ cm/s}$. The maximum value of $\approx 4 \text{ cm/s}$ is achieved in the seventh band when $\nu_{\text{ex}} \in 10\text{--}15 \text{ Hz}$.

■ DISCUSSION

Three key outputs of the thin layer of BZ reaction when subjected to acoustic waves allow the discrimination of seven bands within the 10–2000 Hz range. One output is the dependence of the AIPWs' velocity on ν_{ex} , which is shown in Figure 8a. It can be fitted by a biexponential decay function of the type

$$\bar{v}_{\text{AIPW}} = (\bar{v}_{\text{AIPW}})_0 + e^{-\nu_{\text{ex}}/\nu_1} + e^{-\nu_{\text{ex}}/\nu_2} \quad (10)$$

where $\nu_1 = 14.7$ Hz and $\nu_2 = 374.5$ Hz, as shown in Figure S27. The first exponential term describes the steep decay of \bar{v}_{AIPW} when ν_{ex} changes from 10 to 50 Hz, i.e., when we move from band VII to band VI. The second exponential term describes the much more gradual decay of \bar{v}_{AIPW} when ν_{ex} changes from 50 to 600 Hz, i.e., when we move from band VI to band II.

The second output that contributes to the discrimination of the seven acoustic bands consists of spatiotemporal patterns generated by the BZ reaction in response to the acoustic frequencies. A summary of all the spatiotemporal patterns is shown and reported in Figure 8b. The top panel of Figure 8b shows a sequence of eight snapshots, which are representative of the typical patterns emerging when the reaction is unperturbed (at the far right of the sequence) and when it is subjected to frequencies within the seven acoustic bands described above (from right to left). The graph below the snapshots depicts the frequencies of the different types of chemical waves as functions of ν_{ex} . The seven bands defined in this work have fuzzy boundaries: the transition from one kind of response to another is not abrupt but gradual. The first band (I) exhibits spontaneous phase waves (PWs), sparse target patterns (STPs), and dense target patterns (DTPs), similar to the unperturbed BZ reaction, with the DTPs having about three times higher frequencies (of the order of 0.035 Hz) than the STPs and PWs. ν_{DTP} is even larger than the color change frequency of the same reaction carried out in a beaker under magnetic stirring ($\nu_{\text{StirredBZ}} = 0.022$ Hz). In the second band (II), the PWs and the DTPs persist, and the first examples of advection-induced phase waves (AIPWs) appear. The AIPWs and DTPs have comparable frequencies (larger than 0.03 Hz). In the third band (III), spontaneous PWs disappear completely. For $\nu_{\text{ex}} \leq 390$ Hz, only AIPWs are detected: their spatiotemporal evolution and formation frequency (ν_{AIPW}) are complex functions of ν_{ex} . They depend on the topography of the thin layer of the solution, which is ruled by the Faraday patterns. Sound-induced Faraday patterns have been exploited as templates to assemble floating beads in programmable patterns,³³ for the programmable movement of floating cargos,³³ for aligning supramolecular nanofibers,³⁴ and for controlling redox-sensitive, pH-sensitive,³⁵ and cascade reactions³⁶ due to the nonuniform dissolution, diffusion, and transport of gaseous reactants through the air–water interface. It is well-known that the BZ reaction is affected by the air–water interface because it involves gaseous oxygen and bromine in its multistep mechanism.^{37,38} The dependence of the Faraday waves' wavelength (λ_{FW}) on the vibrational driving frequency (ν_{ex}) reported in eq 2 and shown in Figure S2A constitutes the third output that, combined with the other two mentioned above, allows the discrimination of the seven acoustic bands in the 10–2000 Hz range.

■ CONCLUSIONS

The results described in this work show that a thin layer of the BZ reaction subjected to audible vertical vibration can serve as a sort of bioinspired, chemo-acoustic system. Analogously to the human ear, where the cochlea transduces mechanical energy into electrochemical energy and topographic representations of the acoustic waves are generated along the basilar membrane, the BZ solution transduces mechanical energy into chemical energy, and distinct spatiotemporal patterns are generated as representations of the seven acoustic bands in the range 10–2000 Hz. A thin layer of the BZ reaction might serve as a tool for hearing-impaired people, who could infer single low-frequency acoustic bands by looking at the vibrationally induced spatiotemporal chemo-patterns. It is evident that the chemo-acoustic BZ system is not nearly as efficient and refined as the human cochlea: its response frequencies ($\nu_{\text{Chem. Waves}}$) are slow compared to the applied acoustic frequencies ($\nu_{\text{Chem.Waves}}/\nu_{\text{ex}} \leq 4.5 \times 10^{-3}$), and its behavior when multiple acoustic frequencies are applied in parallel remains to be investigated. Perhaps, the BZ reaction in a Petri dish may become a useful tool in neuromorphic engineering if it can be shown that it transduces inaudible infrasounds into easily visible spatiotemporal chemo-patterns.

■ ASSOCIATED CONTENT

SI Supporting Information

The Supporting Information is available free of charge at <https://pubs.acs.org/doi/10.1021/acs.jpcb.3c08429>.

Sketch of the experimental setup; figures relative to the computational section; sync conditions in the unperturbed system and when $\nu_{\text{ex}} = 680, 634, 390$, and 130 Hz; spatiotemporal patterns of the unperturbed system and when $\nu_{\text{ex}} = 609, 564, 500, 463, 360, 270, 115, 97, 53, 24, 18$, and 15 Hz; nodes and antinodes in the 500–650 Hz range; and amplitude of vertical mechanical vibration as a function of ν_{ex} ([PDF](#))

Ten-times-accelerated video of the unperturbed BZ reaction (E0) ([MP4](#))

Ten-times-accelerated video when subjected to an acoustic frequency of $\nu_{\text{ex}} = 680$ Hz (E1) ([MP4](#))

Ten-times-accelerated video when subjected to an acoustic frequency of $\nu_{\text{ex}} = 634$ Hz (E2) ([MP4](#))

Ten-times-accelerated video when subjected to an acoustic frequency of $\nu_{\text{ex}} = 390$ Hz (E3) ([MP4](#))

Ten-times-accelerated video when subjected to an acoustic frequency of $\nu_{\text{ex}} = 130$ Hz (E4) ([MP4](#))

Ten-times-accelerated video when subjected to an acoustic frequency of $\nu_{\text{ex}} = 72$ Hz (E5) ([MP4](#))

Ten-times-accelerated video when subjected to an acoustic frequency of $\nu_{\text{ex}} = 32$ Hz (E6) ([MP4](#))

Ten-times-accelerated video when subjected to an acoustic frequency of $\nu_{\text{ex}} = 10$ Hz (E7) ([MP4](#))

■ AUTHOR INFORMATION

Corresponding Author

Pier Luigi Gentili – Department of Chemistry, Biology, and Biotechnology, Università degli Studi di Perugia, 06123 Perugia, Italy; orcid.org/0000-0003-1092-9190; Email: pierluigi.gentili@unipg.it

Authors

Laura Tomassoli — Department of Chemistry, Biology, and Biotechnology, Università degli Studi di Perugia, 06123 Perugia, Italy

Leonardo Silva-Dias — Department of Chemistry, Brandeis University, Waltham, Massachusetts 02454-9110, United States; Department of Chemistry, Federal University of São Carlos, São Carlos, São Paulo 13.565-905, Brazil;

orcid.org/0000-0003-0535-6666

Milos Dolnik — Department of Chemistry, Brandeis University, Waltham, Massachusetts 02454-9110, United States

Irving R. Epstein — Department of Chemistry, Brandeis University, Waltham, Massachusetts 02454-9110, United States; orcid.org/0000-0003-3180-4055

Raimondo Germani — Department of Chemistry, Biology, and Biotechnology, Università degli Studi di Perugia, 06123 Perugia, Italy

Complete contact information is available at:

<https://pubs.acs.org/10.1021/acs.jpcb.3c08429>

Notes

The authors declare no competing financial interest.

ACKNOWLEDGMENTS

P.L. Gentili, R. Germani, and L. Tomassoli thank A. Nicoziani for assembling the Petri dish/vertical vibrations generator, M. Menichetti for writing the software to extract RGB values from the pixels of the recorded videos, F. Nicoletti for initial experimental support, and Prof. F. Cottone for the determination of the oscillation amplitudes at the different acoustic frequencies. This work was supported by the European Union-NextGenerationEU under the Italian Ministry of University and Research (MUR) National Innovation Ecosystem grant ECS00000041-VITALITY. P.L.G. acknowledges Università degli Studi di Perugia and MUR for support within the project Vitality. I.R.E. and M.D. were supported by grant CHE-1856484 from the National Science Foundation. L. Silva-Dias thanks the Brazilian funding agencies Fundação de Amparo à Pesquisa do Estado de São Paulo (FAPESP; grants 2022/00257-0 and 2019/23205-3) and Coordenação de Aperfeiçoamento de Pessoal de Nível Superior (CAPES), finance code 001.

REFERENCES

- (1) Schwab, K. *The Fourth Industrial Revolution*. Crown Business, New York, 2016.
- (2) Kurzweil, R. *The singularity is near*. Palgrave Macmillan UK, 2014.
- (3) Christensen, D. V.; Dittmann, R.; Linares-Barranco, B.; Sebastian, A.; Le Gallo, M.; Redaelli, A.; Slesazeck, S.; Mikolajick, T.; Spiga, S.; Menzel, S.; et al. 2022 roadmap on neuromorphic computing and engineering. *Neuromorph. Comput. Eng.* **2022**, 2 (2), No. 022501.
- (4) Nawrocki, R. A.; Voyles, R. M.; Shaheen, S. E. A Mini Review of Neuromorphic Architectures and Implementations. *IEEE Trans. Electron Devices* **2016**, 63, 3819–3829.
- (5) Lee, Y.; Lee, T. W. Organic Synapses for Neuromorphic Electronics: From Brain-Inspired Computing to Sensorimotor Nervetronics. *Acc. Chem. Res.* **2019**, 52, 964–974.
- (6) Zhu, J.; Zhang, T.; Yang, Y.; Huang, R. A comprehensive review on emerging artificial neuromorphic devices. *Appl. Phys. Rev.* **2020**, 7, No. 011312.

(7) Wang, Z.; Wu, H.; Burr, G. W.; Hwang, C. S.; Wang, K. L.; Xia, Q.; Yang, J. J. Resistive switching materials for information processing. *Nature Rev. Mater.* **2020**, 5, 173–195.

(8) Mao, L. Neuromorphic Sensing: A New Breed of Intelligent Sensors. *ACS Sens.* **2023**, 8, 2896–2897.

(9) Gentili, P. L.; Stano, P. Tracing a new path in the field of AI and robotics: mimicking human intelligence through chemistry. Part I: molecular and supramolecular chemistry. *Front. Robot. AI* **2023**, 10, 1238492.

(10) Gentili, P. L.; Stano, P. Tracing a new path in the field of AI and robotics: mimicking human intelligence through chemistry. Part II: systems chemistry. *Front. Robot. AI* **2023**, 10, 1266011.

(11) Gorecki, J.; Giziński, K.; Guzowski, J.; Gorecka, J. N.; Garstecki, P.; Gruenert, G.; Dittrich, P. Chemical computing with reaction–diffusion processes. *Philos. Trans. R. Soc. A* **2015**, 373, 20140219.

(12) Proskurkin, I. S.; Smelov, P. S.; Vanag, V. K. Experimental verification of an opto-chemical “neurocomputer. *Phys. Chem. Chem. Phys.* **2020**, 22, 19359–19367.

(13) Gentili, P. L.; Giubila, M. S.; Germani, R.; Romani, A.; Nicoziani, A.; Spalletti, A.; Heron, B. M. Optical Communication among Oscillatory Reactions and Photo-Excitable Systems: UV and Visible Radiation Can Synchronize Artificial Neuron Models. *Angew. Chem., Int. Ed.* **2017**, 56, 7535–7540.

(14) Gentili, P. L.; Horvath, V.; Vanag, V. K.; Epstein, I. R. Belousov-Zhabotinsky ‘chemical neuron’ as a binary and fuzzy logic processor. *Int. J. Unconv. Comput.* **2012**, 8, 177–192.

(15) Okamoto, H.; Tanaka, N.; Naito, M. Analogy between the stimulus-response characteristics of neuronal and electrochemical cells. *Chem. Phys. Lett.* **1995**, 237, 432–436.

(16) Ling, H.; Koutsouras, D. A.; Kazemzadeh, S.; van de Burgt, Y.; Yan, F.; Gkoupidenis, P. Electrolyte-gated transistors for synaptic electronics, neuromorphic computing, and adaptable biointerfacing. *Appl. Phys. Rev.* **2020**, 7, No. 011307.

(17) Nakano, T. Molecular Communication: A 10 Year Retrospective. *IEEE Trans. Mol. Biol. Multi-Scale Commun.* **2017**, 3, 71–78.

(18) Nakano, T.; Suda, T. Molecular Communication Using Dynamic Properties of Oscillating and Propagating Patterns in Concentration of Information Molecules. *IEEE Trans. on Commun.* **2017**, 65, 3386–3398.

(19) Zaikin, A. N.; Zhabotinsky, A. M. Concentration Wave Propagation in Two-dimensional Liquid-phase Self-oscillating System. *Nature* **1970**, 225, 535–537.

(20) Scott, S. K. *Oscillations, waves, and chaos in chemical kinetics*. Oxford University Press, Oxford, 1994.

(21) Hsu, T. J.; Mou, C. Y.; Lee, D. J. Effects of Macromixing on the Oregonator model of the Belousov — Zhabotinsky reaction in a stirred reactor. *Chem. Eng. Sci.* **1994**, 49, 5291–5305.

(22) Epstein, I. R.; Pojman, J. A. *Introduction to Nonlinear Chemical Dynamics*. Oxford University Press, New York, 1998.

(23) Pickles, J. *An Introduction to the Physiology of Hearing*. Academic Press, London, 1988.

(24) Hudspeth, A. J. How the ear’s works work. *Nature* **1989**, 341, 397–404.

(25) Gentili, P. L. The human sensory system as a collection of specialized fuzzifiers: A conceptual framework to inspire new artificial intelligent systems computing with words. *J. Intell. Fuzzy Syst.* **2014**, 27, 2137–2151.

(26) Faraday, M., XVII On a peculiar class of acoustical figures; and on certain forms assumed by groups of particles upon vibrating elastic surfaces. *Philos. Trans. R. Soc.* **1831**, 121, 299–340.

(27) Wright, P. H.; Saylor, J. R. Patterning of particulate films using Faraday waves. *Rev. Sci. Instrum.* **2003**, 74, 4063–4070.

(28) Fernández-García, G.; Roncaglia, D. I.; Pérez-Villar, V.; Muñozuri, A. P.; Pérez-Muñozuri, V. Chemical-wave dynamics in a vertically oscillating fluid layer. *Phys. Rev. E* **2008**, 77, No. 026204.

(29) von Kameke, A.; Huhn, F.; Fernández-García, G.; Muñozuri, A. P.; Pérez-Muñozuri, V. Propagation of a chemical wave front in a

quasi-two-dimensional superdiffusive flow. *Phys. Rev. E* **2010**, *81*, No. 066211.

(30) Adamatzky, A. A brief history of liquid computers. *Philos. Trans. R. Soc. B* **2019**, *374*, 20180372.

(31) Tyson, J. J.; Fife, P. C. Target patterns in a realistic model of the Belousov–Zhabotinskii reaction. *J. Chem. Phys.* **1980**, *73*, 2224–2237.

(32) Levenspiel, O. *Chemical Reaction Engineering*. John Wiley & Sons, New York, 1972.

(33) Choi, S.; Mukhopadhyay, R. D.; Sen, S. K.; Hwang, I.; Kim, K. Out-of-equilibrium chemical logic systems: Light-and sound-controlled programmable spatiotemporal patterns and mechanical functions. *Chem.* **2022**, *8*, 2192–2203.

(34) Tsuda, A.; Nagamine, Y.; Watanabe, R.; Nagatani, Y.; Ishii, N.; Aida, T. Spectroscopic visualization of sound-induced liquid vibrations using a supramolecular nanofibre. *Nat. Chem.* **2010**, *2*, 977–983.

(35) Hwang, I.; Mukhopadhyay, R. D.; Dhasaiyan, P.; Choi, S.; Kim, S. Y.; Ko, Y. H.; Baek, K.; Kim, K. Audible sound-controlled spatiotemporal patterns in out-of-equilibrium systems. *Nat. Chem.* **2020**, *12*, 808–813.

(36) Dhasaiyan, P.; Ghosh, T.; Lee, H. G.; Lee, Y.; Hwang, I.; Mukhopadhyay, R. D.; Park, K. M.; Shin, S.; Kang, I. S.; Kim, K. Cascade reaction networks within audible sound induced transient domains in a solution. *Nature Comm.* **2022**, *13*, 2372.

(37) Steinbock, O.; Hamik, C. T.; Steinbock, B. Oxygen Inhibition of Oscillations in the Belousov–Zhabotinsky Reaction. *J. Phys. Chem. A* **2000**, *104*, 6411–6415.

(38) Kalishyn, Y. Y.; Rachwalska, M.; Khavrus, V. O.; Strizhak, P. E. The effect of oxygen on time-dependent bifurcations in the Belousov–Zhabotinsky oscillating chemical reaction in a batch. *Phys. Chem. Chem. Phys.* **2005**, *7*, 1680–1686.